Geologica Acta, Vol.8, Nº 1, March 2010, 31-49
DOI: 10.1344/105.000001514
Available online at www.geologica-acta.com

geologica acta

On processing of Controlled Source Electromagnetic (CSEM) Data

OLEG V. PANKRATOV [1] [*] **and ALEXEY I. GERASKIN** [2]

[1] **Institute of Terrestrial Magnetism, Ionosphere and Radio Wave Propagation of Russian Academy of Science**
142190, Troitsk, Moscow region, Russia, and Nord-West Limited, 117546, Ul. Podolskikh Kursantov, 24D, Moscow, Russia.
E-mail: oleg.pankratov@gmail.com

[2] **Nord-West Limited**
117546, Ul. Podolskikh Kursantov, 24D, Moscow, Russia. E-mail: alexey.geraskin@gmail.com

* corresponding author E-mail: oleg.pankratov@gmail.com

ABSTRACT

In this paper, we present a fast and robust scheme of controlled source electromagnetic data processing. We specify in detail various types of noise that affect measurements and show how these noise components can be suppressed. We promote an improved algorithm to process noisy data. We demonstrate that our method can recover response functions from extremely noisy field data. The proposed software can be adapted to new data sets and noisy environments. We apply our processing method to field data from Kola Peninsula, Norilsk region and Pechora province (Russia).

KEYWORDS | **Controlled source electromagnetics. Robust processing. Response functions. Phase difference.**

INTRODUCTION

Controlled source electromagnetic (CSEM) methods (e.g., Zhdanov and Keller, 1994) are generalizations of well known direct current (DC) methods of electric sounding of the Earth (e.g., Koefoed, 1979). CSEM methods have several advantages over DC methods, the most significant being that CSEM signal penetrates through resistive screens due to the inductive mode of the electromagnetic (EM) field. Compared to the magnetotelluric (MT) method (e.g., Simpson and Bahr, 2005), CSEM methods have one more advantage: they can be used in areas with a high level of industrial or natural noise.

While the magnetotelluric (MT) method uses natural electromagnetic variations of source, CSEM uses a controlled (known) variation of source. However, the processing of CSEM data is a challenging task due to the high noise/signal ratio which may reach three orders of magnitude, as we will see below. In this paper, we present fast and robust processing procedures that allow suppression of a variety of noises and result in reliable response functions. Though long offset transient electromagnetic (LOTEM) data processing described by Strack et al. (1989) resembles CSEM processing in many aspects, it differs from the latter as the variety of CSEM cases are numerous, depending mainly on the following factors: field set-up

(source-to-receiver offset, etc.), response function type (electric, magnetic, time-domain, frequency-domain, amplitude, phase difference, etc.), source signal waveform and period, sampling interval, latitude of the observation area, and intensity and character of cultural noise (Edwards and Nabighian (1991), Spies and Frischknecht (1991), Nabighian and Macnae (1991), Zonge and Hughes (1991), Chave et al. (1991), Velikhov (1989), Pushkarev and Yakovlev (2005)). In each case, some suitable algorithm corrections needed to be made, hence we constructed a group of operations and universal processing software based on this group. We have been applying the software to several fieldwork data sets since 2004 (particularly, 1280 km of resistivity and induced polarization profiles in 2007) and we performed the necessary modifications to the algorithm according to the survey using the group of operations.

TYPES OF CSEM SIGNAL

In CSEM surveys, the Earth's response is excited by the source signal. The latter is created by the transmitter which is a combination of a generator, feeders, grounded dipoles, wire loops or induction coils.

Types of source signal

The source signal is a time series of electric current produced by the generator. As usual, the source signal waveform is either a square-wave (Fig. 1A) or a pulsed square-wave (Fig. 1C). Source signal can be considered as a carrier signal. The Earth's response can be considered as a small addition to the carrier that is schematically shown in Figs. 1B,D for two source signal waveforms. The source signal, as well as the Earth's response, has a line spectrum.

Response signal seen in raw data

Raw data examples are shown in Figs. 2-8. It is often difficult to recognize the Earth's response in raw time series. The goal of our processing algorithms is the reliable and robust extraction of the Earth's responses from the data.

Types of response functions

Response function can be a function of either time or frequency. In the latter case, the square-wave is mostly used (Fig. 1A) as the source signal, and we obtain the complex Fourier harmonics (see eq. (24)), $C_1, C_3, C_5, \ldots$, of the response (Fig. 1B), their absolute values,

$$A_1, A_3, A_5, \ldots, \quad (1)$$

and phases,

$$\varphi_1, \varphi_3, \varphi_5, \ldots . \quad (2)$$

Complex Fourier harmonics are the coefficients of the Fourier series of the signal which has a period T (see eq. (10)). Complex amplitudes of even harmonics are equal to zero due to antiperiodicity (see eq. (9)). As a response function, the so called percent frequency effect (PFE) is often used, which is defined (Sheriff, 2002) as

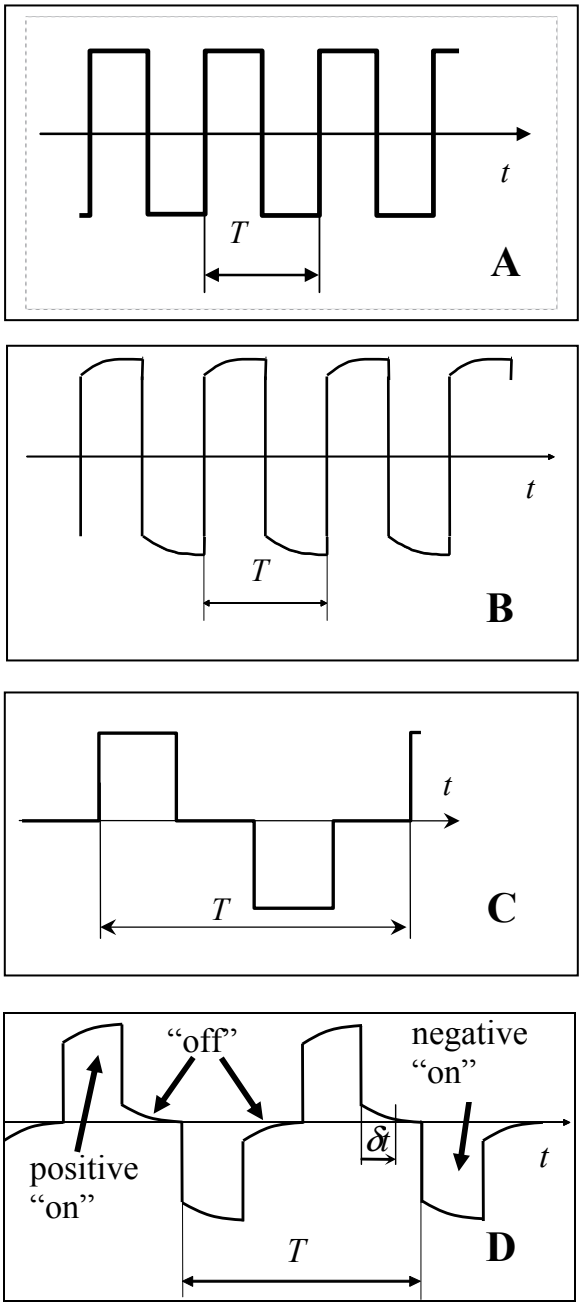

FIGURE 1 | **Source signal waveforms: A) square-wave, B) pulsed square-wave. Signal at the receiver is the source carrier signal with Earth's response: C) for square-wave, and D) for pulsed square-wave, here *t* stands for time, δt stands for time delay within the "off" quarter-period.**

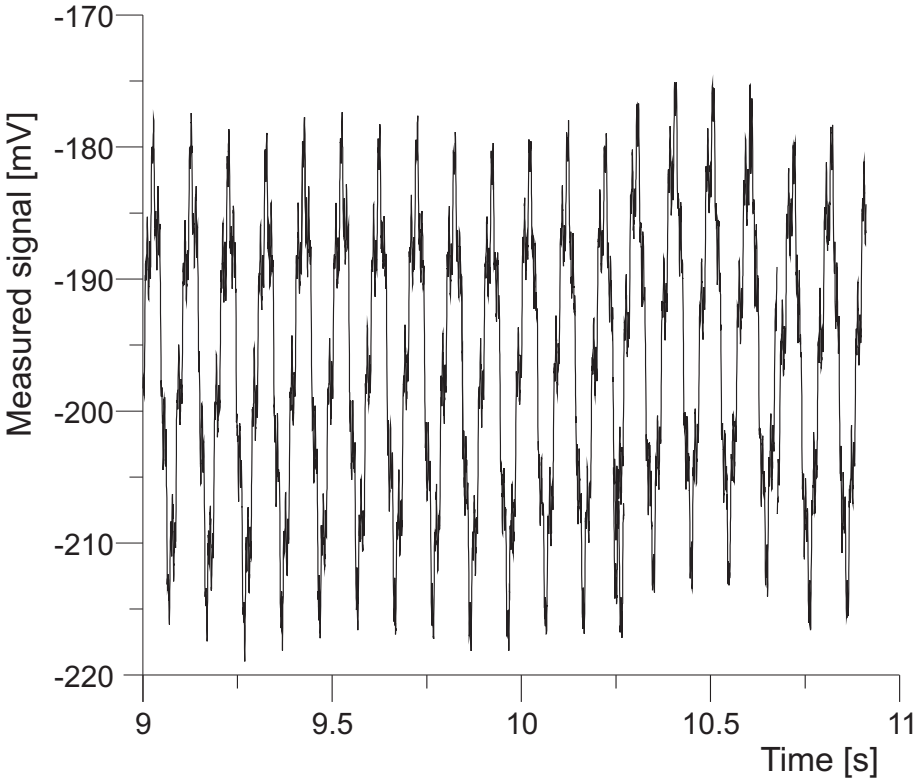

FIGURE 2 | **Industrial noise: ~50 Hz.**

$$PFE = \frac{mA_m - nA_n}{nA_n} \cdot 100\ \%\,, \qquad (3)$$

where, m,n = 1,3,5,… . Another example of the response function used in CSEM sounding is the phase difference which is obtained by

$$\Delta\varphi_{n,m} = -\frac{n\varphi_m - m\varphi_n}{n-m} - \frac{\pi}{2}\left(\mathrm{mod}\,\frac{2\pi}{n-m}\right). \qquad (4)$$

Here, we take time dependency in the form of $e^{-i\omega t}$ (cf. Kulikov et al., 1975). The term -π/2 is responsible for the primary field square-wave (Fig 1A). The expression X(mod Y) stands for the remainder of division of X by Y. (Note that the "minus" sign in front of the fraction in (4) changes to "plus" if we replace the exponential factor $e^{-i\omega t}$ by $e^{i\omega t}$). The phase difference is mostly used to study induced polarization of rocks. A merit of the phase difference is that its calculation doesn't require hardware- or software-based synchronization between transmitter and receivers. The phase difference is defined by Kulikov et al. (1975) as

$$\Delta\varphi(\omega_1,\omega_2) = -\frac{\omega_1\varphi(\omega_2) - \omega_2\varphi(\omega_1)}{\omega_1 - \omega_2}. \qquad (5)$$

However, this formula is not convenient for field data processing as it is relative to the origin (when t = 0) and because it does not take into account the primary carrier square-wave, which is represented by the term -π/2 in eq. (4). On the contrary, eq. (4) can easily be applied to the Fourier coefficients that are derived from the raw time series, irrespective of the source/receiver synchronization and the correction for source signal in the measured signal. The phase difference (4) is mostly used for frequencies from 0.01 Hz to 10 Hz since the lower frequency data are too long to obtain, and higher frequency data are mostly due to induction rather than IP. Furthermore, the value of the phase difference, $\Delta\varphi_{1,3}$, over a typical ore deposit ranges from -0.5° to -5° or even more. It has been found experimentally (see Kulikov and Shemyakin, 1978, and Pushkarev and Yakovlev, 2005) that phase difference $\Delta\varphi_{1,3}$ at frequencies of 0.1-1 Hz varies only slightly and is linked to IP chargeability at a 0.5 s delay as follows:

$$\eta\,[\%] = -2.5\,\Delta\varphi_{1,3}\,[^\circ]. \qquad (6)$$

Our field tests show that the phase difference response (e.g., Fig. 9) is numerically stable: typical RMS scatter is about 0.001°, therefore the phase difference is highly accurate. Apparent resistivity may also be obtained using the equation (Zhdanov and Keller, 1994)

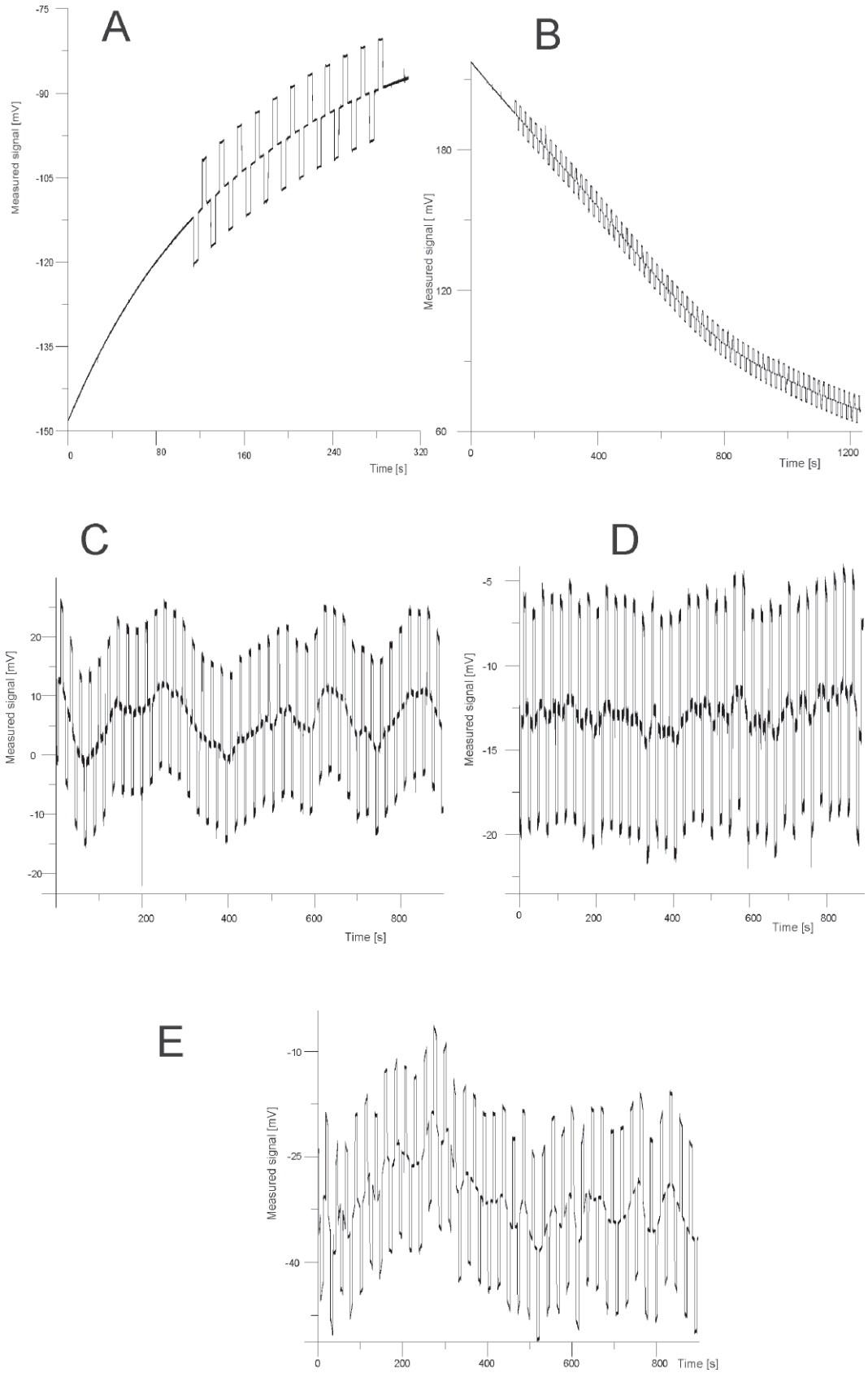

FIGURE 3 | **Trend types: A) Smooth quasi-polynomial trend. B) Smooth jerky trend. C) Bad trend. D) Worse trend. E) The worst trend.**

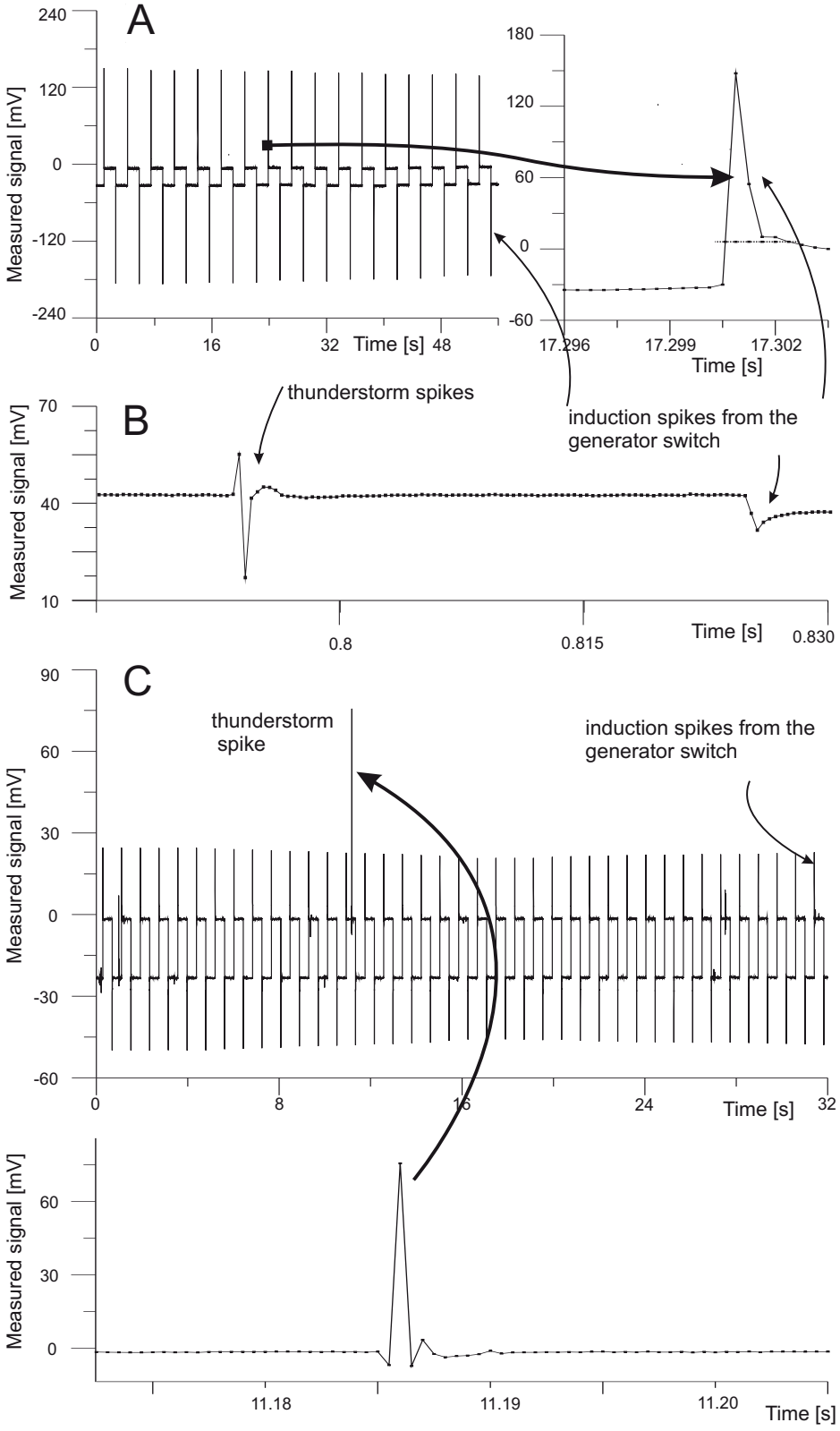

FIGURE 4 | **Spikes: A) spikes arising from the parasitic induction (magnetic and/or electric) at the square-wave fronts of the source signal (switch-on and switch-off moments). Horizontal line at the right panel shows how we substitute "spiked" values with the robust mean in order to reduce the spike. B) Thunderstorm spike and electric/magnetic induction spike at four simultaneously recorded channels of 8-channel equipment RMCIP. Thunderstorm spikes are statistically independent on the source waveform. C) Thunderstorm spikes can have many times larger magnitude than induction spikes, source signal and, a fortiori, than the response sought.**

$$\rho_\omega = \frac{2\pi r^3}{3x^2/r^2 - 2} \cdot \frac{A_x}{IL}, \quad (7)$$

for far field conditions. Here, IL is the source dipole moment, r is the source-to-receiver offset, x is the offset along source grounded wire line AB, A_x is the first harmonic absolute value of the x-component of the voltage measured.

The induced polarization (IP) effect is calculated in the time domain as

$$IP(\delta t) = \frac{V(\delta t)}{V_{\max}} \cdot 100\,\%, \quad (8)$$

where $V(\delta t)$ is the observed voltage across the dipole and $V_{\max}$ is the essential maximum of $|V(\delta t)|$. In the case of a pulsed square-wave, the variable δt in eq. (8) stands for the time within the "off" quarter-period of the pulsed square-wave (Fig. 1D).

Types of noise

Measured CSEM data are generally noisy. Noise types are as follows: industrial noise (mainly 50 Hz or 60 Hz (Fig. 2)), trends (Fig. 3) and spikes due to thunderstorms (Figs. 4B,C). Trends can be smooth (polynomial (Fig. 3A), jerky (Fig. 3B)) or rough (Figs. 3C-E). Trends are the most difficult noise to remove. In addition, there are other distortions arising from parasitic induction (Fig. 4A).

OTHER SURVEY DETAILS

Equipment and transmitter-receiver set-up

The CSEM method can use any of the transmitter-receiver set-ups which are traditionally used by DC methods, viz Resistance, Schlumberger, Wenner, dipole-dipole, pole-dipole, pole-pole, azimuthal, self-

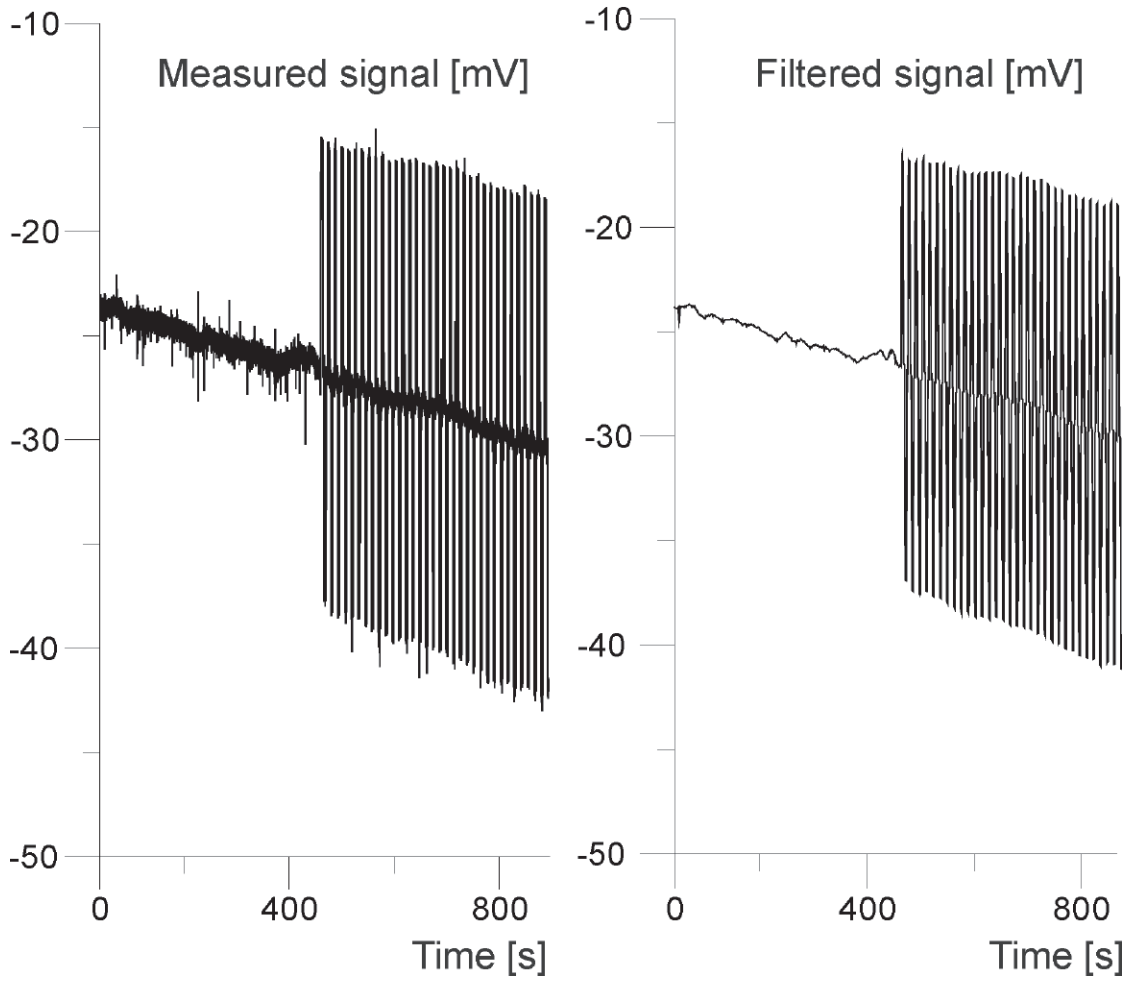

FIGURE 5 | **The suppression of industrial noise. Left panel: before industrial noise suppression. Right panel: after industrial noise suppression.**

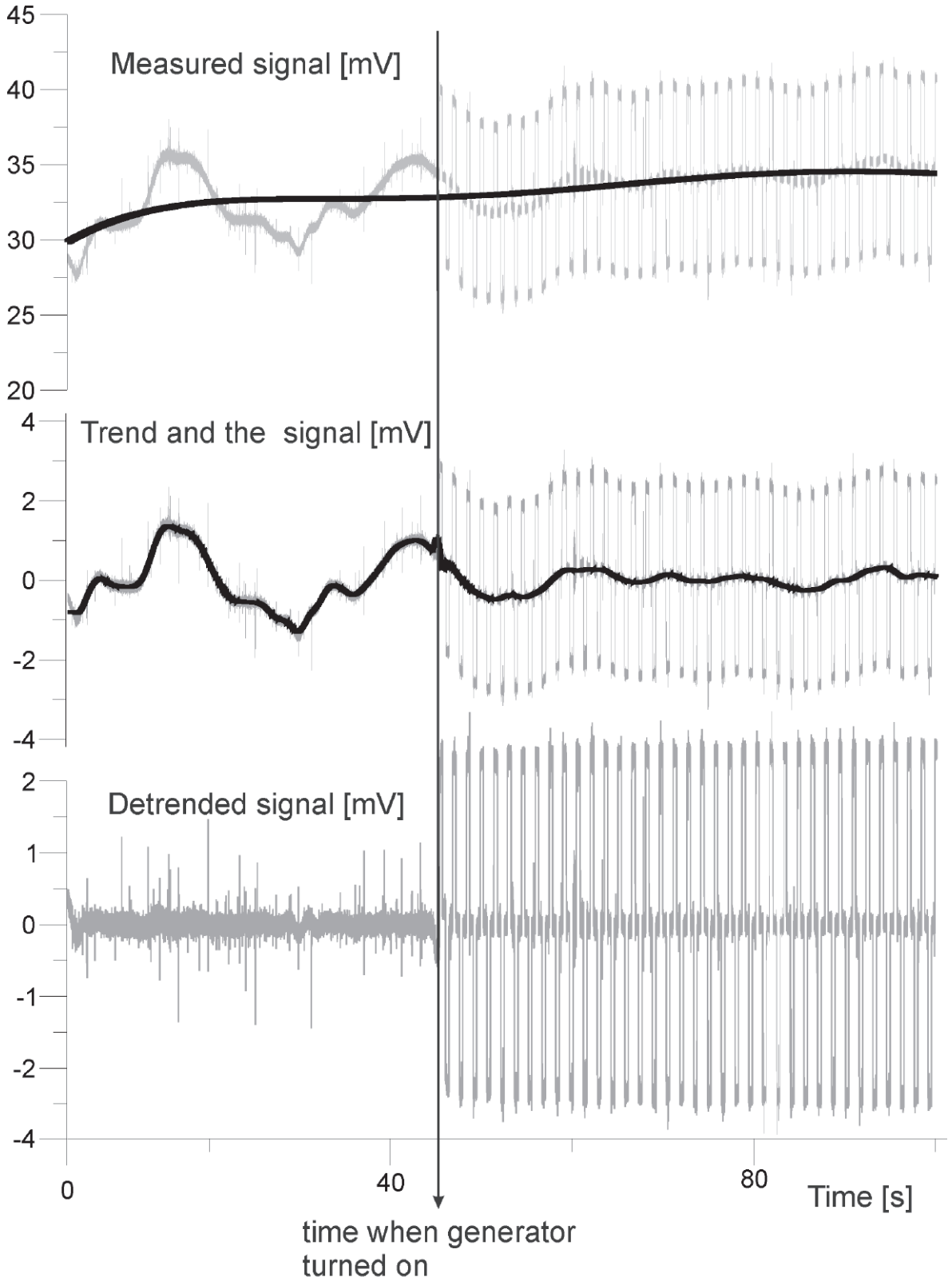

FIGURE 6 | **Illustration of trend suppression. Upper panel: gray signal represents raw data, black signal represents polynomial trend estimate. Middle panel: gray signal represents raw data with polynomial trend removed, black signal is gray signal running mean that is considered a better estimate of the trend. Lower panel: the resulting signal with trends suppressed. Vertical arrow across the graphs shows the time when generator was turned on. Even horizontal noise to the left of the arrow at the lower panel verifies the degree of accuracy of the trend removal, besides that, it is seen in the lower panel that the source signal amplitude drifts slowly.**

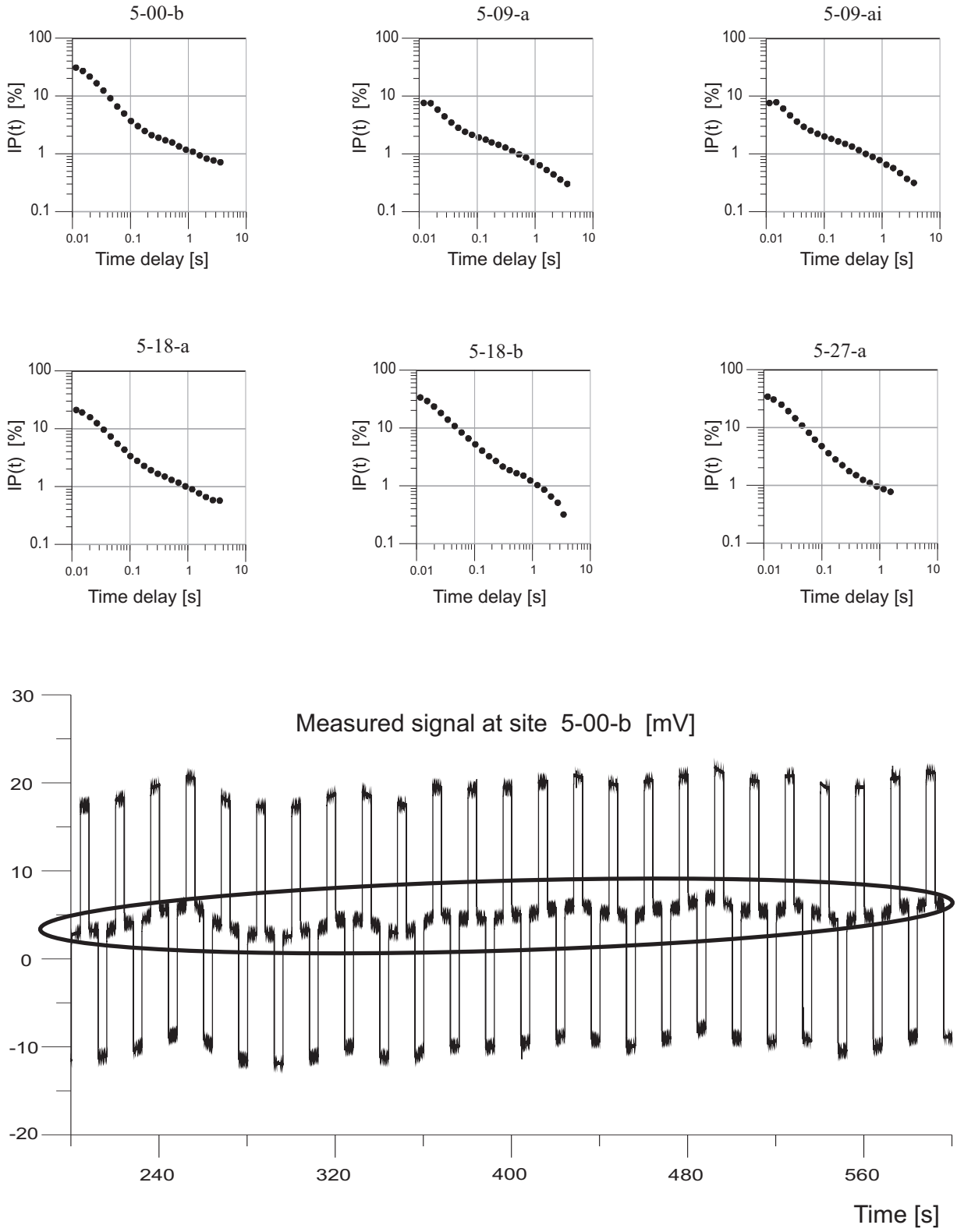

FIGURE 7 | **Upper panel: responses (see eq. (8)) at 6 observation sites of an IP-DNM profile. The responses are presented in log-log scale and drop down 2.5 orders of magnitude with time delay changing from 0.01 s to 4 s. Source signal type is pulsed square-wave. The responses are obtained from the "off" quarter-periods measurements (when the source signal equals zero). The zero time delay corresponds to the beginning of the "off" quarter-period. Lower panel: raw data obtained at the observation site "5-00-b" (shown left at upper panel). Encircled data "spots" depict the measured signal in the "off" quarter-periods which has been used to recover the response function at the upper left log-log plot.**

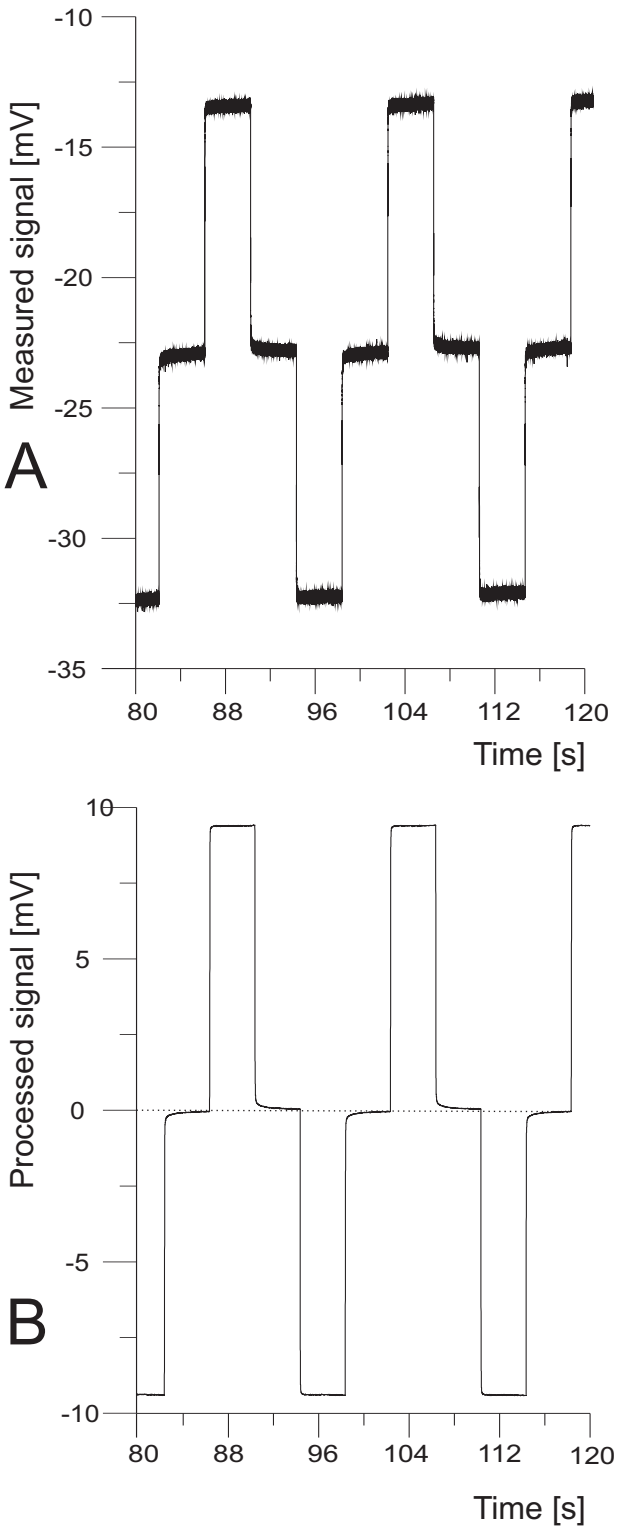

FIGURE 8 | **Sometimes it turns out that the measured signal is rather good. Upper panel: measured signal. Lower panel: processed CSEM time-domain signal in linear scale.**

potential (SP) gradient, etc. Additionally, loop measurement can be performed (loop-loop, loop-dipole, dipole-loop). In the figures below, we will show the data acquired with the use of the IP-central-gradient set-up (Fig. 10A) and with the use of the differential-normalized method (DNM, see Davydycheva et al., 2006) set-up (Fig. 10B).

There exists a large variety of equipment to be used for CSEM surveys. We used the equipment *MTU-5A* (Phoenix Geophysics Limited, http://www.phoenix-geophysics.com) and equipment *RMCIP* and *MARY-24* (Nord-West Limited, http://www.nw-geo.ru/index_en.php?a=2&c=5 and http://www.nw-geo.ru/index_en.php?a=1&b=2&c=2) for our surveys.

Survey areas

Nord-West Limited performed several CSEM surveys: 1) on the Kamchatka Peninsula, 2) on the Kola Peninsula, 3) in Aikhal (Alekseev et al., 2006), 4) near Pechora, 5) near Norilsk, and 6) in the Northern Urals. Each of these measurements was affected by different types of noise, which makes it necessary to use different processing algorithms to remove the noise in each scenario.

PROCESSING ALGORITHMS

Basic property of the signal

Antiperiodicity is a basic property of the signal, designed as

$$S\left(t+T/2\right)=-S\left(t\right), \tag{9}$$

where T is the period of source signal (which in turn depends on the measurement settings). Both t and $t + T/2$ have to be within a single generator run. The periodicity property

$$S\left(t+T\right)=S\left(t\right), \tag{10}$$

is the consequence of (9).

Group of operations

The measured signal, $M(t)$, is a series of successive samples, $M(t_{start})$, $M(t_{start} + \Delta t)$, $M(t_{start} + 2\Delta t)$, … , $M(t_{finish})$, where t_{start} is the first reading time of the series, t_{finish} is the last reading time of the series, $\Delta t=1/f_s$ is the sample interval in s, and f_s is the sampling frequency in Hz. Duration t_{finish} - t_{start} is referred to as the duration of the measurement of the signal $M(t)$. Time interval (t_{start}, t_{finish}) is referred to as the measurement time interval of signal $M(t)$. We construct the processing algorithm as a composition of a series of operations,

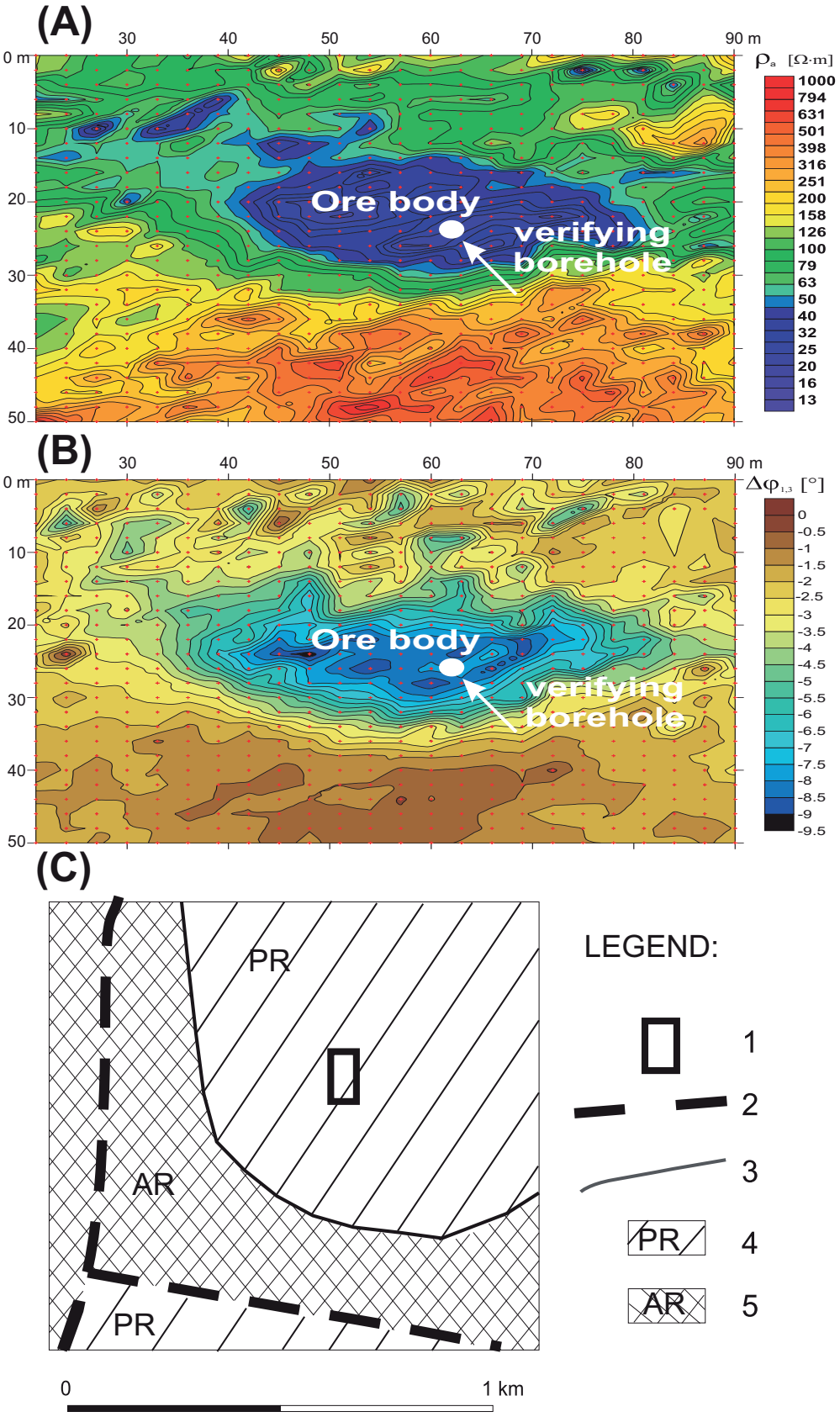

FIGURE 9 | **A) IP resistivity and B) phase difference ($\Delta\varphi_{1,3}$) maps indicate sharp local anomaly at Tsaga massif in Kola Peninsula. Later drilling revealed deep massive ore deposit was at a depth of 6 m below the point shown in white. C) Geological sketch map. Key: 1. survey area, 2. tectonic disruptions, 3. geological boundaries, 4. Proterozoic (gabbro), 5. Archean (granite).**

$$\text{Algorithm}(M) = \text{Op}_1\left(\text{Op}_2\left(...\text{Op}_k\left(M\right)\right)\right) \quad \text{Op} \quad \text{Op} \quad ... \quad \text{Op}$$
$$= \text{Op}_1 \circ \text{Op}_2 \circ ... \circ \text{Op}_k\left(M\right), \qquad (11)$$

to be applied to the measured signal $M(t)$. Each operation Op_i in eq. (11) can be applied to signal $M(t)$ and must output a time series of the same nature as its input. However, the first and last reading times of the output may differ from those of the input. Finally we get a group of operations $\{\text{Op}_i\}_i$ with respect to the composition of operations, " $\circ$ " which is associative. Although the group as a whole is non-commutative, it has large commutative subgroups (e.g., a subgroup of convolution-type operations) which is important as we test, compare, and adjust the algorithms to a survey dataset. For example, the linear filtering operation commutes with the differential accumulation operation but does not commute with the robust differential accumulation described in the next section. We consider the measured signal, $M(t)$, as a superposition of the true signal, $S(t)$; a distortion, $D(t)$; and arbitrary noise, $N(t)$:

$$M\left(t\right) = S\left(t\right) + D\left(t\right) + N\left(t\right). \qquad (12)$$

A distortion is an undesired change in waveform caused by measuring equipment (transmitter, data logger, feeders, electrodes, etc.) which correlates mostly with the true signal. Arbitrary noise is an undesired change in waveform caused by external sources and it is mostly independent of the true signal.

True signal, $S(t)$, and distortion, $D(t)$, belong to the class of T-antiperiodic (see eq. (9)) functions of time. Noise, $N(t)$, is assumed to be statistically independent of the true signal. Each operation Op_i in eq. (11) should leave true signal almost intact or at least transform it to the same class of antiperiodic functions. We consider the processing algorithm (11) to be correct if either noise or distortion decrease after each operation and both of them do not increase. Below we describe the basic operations of our processing scheme.

Differential accumulation

First, by relying on (9), we construct an operation of differential accumulation, δ:

$$\delta: \quad M\left(t\right) \mapsto \delta M\left(t\right) = \frac{M\left(t\right) - M\left(t + T/2\right)}{2}. \qquad (13)$$

Operation δ leaves the true signal intact and reduces the noise. However the operation δ decreases the measurement duration of signal, $M(t)$ by $T/2$: if the measurement time interval of signal, M, is (t_{start}, t_{finish}), then the measurement time interval of signal $\delta(M)$ is interval (t_{start}, t_{finish} - $T/2$). The definitional domain of operation δ is the set of all time series, M, with a measurement duration longer than $T/2$.

Once we have built operation δ, we can apply it many times providing that the measurement duration is sufficiently long. A robust differential accumulation operation has also been designed resembling a selective stacking algorithm described by Strack (1984). The key moment of the robust differential accumulation operation is the robust detrending (see below) of the measured signal and then the application of the differential accumulation using a trimmed mean: $g_{rda} = g_{da} \circ g_{nor} \circ g_{detrend}$, where g_{rda} stands for robust differential accumulation operation, $g_{rda} = \delta^m = \delta \circ ... \circ \delta$ stands for the differential accumulation operation described above, $g_{detrend}$ stands for the detrend operation described below, and g_{nor} stands for following the normalizing operation:

$$g_{nor} = e_t \circ \left(e_{rank}\right)^{-1} \circ e_{normalize} \circ e_{rank} \circ e_{comb}, \qquad (14)$$

where

$$e_{comb}M(t) = (M(t), -M(t + T/2), M(t + T),$$
$$-M(t + 3T/2), ..., (-1)^k M(t + kT/2)). \qquad (15)$$

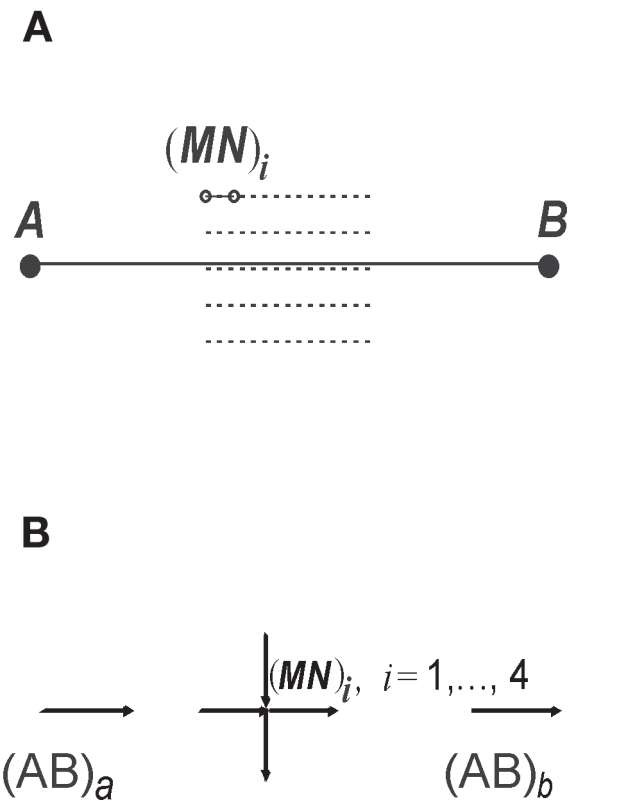

FIGURE 10 | **IP and differential-normalized method fieldwork.**

The e_{rank} operation reorders the input sequence according to rank, the $e_{normalize}$ operation substitutes the q percent of the extreme values with the nearest values, and the $(e_{rank})^{-1}$ reordering operation is the inverse of e_{rank}. Finally, the e_t operation takes the $(k/2)^{th}$ value and attributes it to the time value of $t + k\,T/4$.

Besides the differential accumulation δ^n, one more operation is $h(\delta)$ where h is an arbitrary polynomial satisfying equations $h(0) = 0$, $h(1) = 1$ (to nullify the $T/2$ - periodic components and to preserve the $T/2$ - antiperiodic components of the measured signal, correspondingly). For example, the following operation is often useful for processing:

$$\chi = \frac{(1-\beta+\beta^2-\beta^3+\ldots-\beta^{2m+1})}{(2m+2)}, \qquad (16)$$

where $\beta = 1 - 2\delta$, so that $\beta M(t) = M(t + T/2)$. An equivalent definition for χ reads:

$$\chi M(t) = (2m+2)^{-1} \sum_{k=0}^{2m+1} (-1)^k M(t + kT/2). \qquad (17)$$

Suppression of transient noise

In order to suppress the thunderstorm spikes and other noise with typical duration shorter than carrier period T, we employ robust procedures, such as median, trimmed mean and Hodges-Lehmann estimate (Huber, 1981). As an example, we describe the median operation, μ. Let us choose an odd integer parameter $2L+1 = 1, 3, 5, 7, \ldots$. Let us obtain a series M^L that consists of $2L+1$ samples $M(t-LT)$, $M(t-(L-1)T)$, …, $M(t)$, … , $M(t+(L-1)T)$, $M(t+LT)$ for each reading time $t=t_{start}+k\cdot\Delta t$. Let us calculate the median of these $2L+1$ samples and attribute its value to reading time $t=t_{start}+k\cdot\Delta t$. Let us call the resultant time series $\mu(M)$. Operation μ decreases the measurement duration of signal $M(t)$ by $2LT$. The definitional domain of operation μ is the set of all time series (M) with the measurement duration longer than $2LT$. Once we have built operations δ and μ, we can compose them, providing that the measurement duration is longer than $2LT+T/2$.

Industrial noise suppression

We employ a linear notch filtering operation λ:

$$\lambda : M(t) \mapsto \sum_{y=-N_\Phi}^{N_\Phi} M(t - y\cdot\Delta t)\,\Phi(y\cdot\Delta t) \qquad (18)$$

in order to suppress industrial noise. The value of $2N_\Phi+1$ is the filter length. $\Phi(y\cdot\Delta t)$ are filter coefficients. The filter (Ifeachor and Jervis, 2002) can suppress ~50 Hz frequency or ~60 Hz frequency (depending on the power line frequency of the country). Operation λ decreases the measurement duration of signal $M(t)$ by $2L\cdot\Delta t$. An illustration of industrial noise suppression can be found in Fig. 5. Fig. 11 shows that for the phase IP data the filter influence on the true signal is negligibly small if compared to the typical anomalous value of the phase difference. The same is also true for the amplitude IP data.

Trend suppression

The most difficult task is to remove the trend of time series with lengths smaller than T. We tried several procedures to suppress the trend and we finally adopted an approach based on a running mean which is determined as follows: let the running mean operation, τ, be

$$\tau M(t) = \frac{1}{2N} \sum_{r=-N+1}^{N} M(t - r\cdot\Delta t), \qquad (19)$$

where $2N$ is the number of samples per period of the carrier signal, T,

$$2N = \frac{T}{\Delta t}. \qquad (20)$$

It can be shown that operation τ as applied to the antiperiodic signal gives zero output. Let the detrending operation γ be

$$\gamma = 1 - \tau. \qquad (21)$$

i.e., $\gamma(M)=M-\tau(M)$ for any M. Operation γ leaves the true signal intact because it is antiperiodic. An example of the application of the operation, γ, is given in Fig. 6. Substituting the arithmetic mean in (19) by the trimmed mean, we obtain a robust running mean operation, τ_r, and a robust detrending operation, $\gamma_r=1-\tau_r$. The use of detrend, γ, or robust detrend, γ_r, is of vital importance as it is meaningless to apply ranking to highly trended data. Ranking, in turn, is needed to get robust estimates at sequential steps of the algorithm. The detrend operation decreases the STD value of the data 4-10 times as shown in Fig. 12, where STD is calculated as follows

$$STD(\delta t) = \sqrt{D(K(\delta t))}. \qquad (22)$$

Here δt stands for time delay, $0<\delta t<T$, T is the source signal period, and

$$K(\delta t) = \{K_m(\delta t)\}_{m=m_{start}(\delta t)}^{m_{finish}(\delta t)},$$

$$K_m(\delta t) = M(\delta t + mT), \quad m \begin{cases} m \in \mathbb{Z}, \\ \delta t + mT \in (t_{start}, t_{finish}), \end{cases} t$$

$$D(K(\delta t)) = E\left(\left(K(\delta t) - E(K(\delta t))\right)^2\right),$$

$$E(K(\delta t)) = \frac{1}{m_{finish} - m_{start} + 1} \sum_{s=m_{start}(\delta t)}^{m_{finish}(\delta t)} K_s(\delta t). \qquad (23)$$

For the data in Fig. 12, m_{finish} -m_{start}+1 ≈ 100, t_{finish}-t_{start} ≈ 30 min, T= 16 s.

One special case of distortion

During the fieldwork, it was detected that immediately after switching the source (at short source-receiver offsets) the measured signal shows delta-like spikes (see Fig. 4A). This effect is most probably due to both electric and magnetic induction in the source-Earth-receiver circuit. In order to suppress these spikes, we first roughly evaluated the maximum duration of the spikes (Fig. 4A). Next, we calculated the robust mean of the signal in the following time interval. We then substituted spike-affected values with the robust mean at the current half-period of the meander signal. Finally, we recursively repeated the above steps for all the half-periods. This procedure suppresses the spikes significantly, and since the duration of the spikes is much less than the duration of the period of the meander signal (say, 5-30 spike-affected readings against 2048 readings of the meander period) this procedure only distorts the true signal negligibly.

Fourier transform and frequency domain response functions

The Fourier transform

$$C_k = \frac{1}{N}\sum_{n=1}^{N} M(t_n) e^{2\pi ink/N}, \qquad (24)$$

is used to obtain frequency responses. Here $N=T/\Delta t$, T is the period of the carrier signal, Δt is the sample interval, $t_n = n\Delta t+IT$, and I is an integer. The complex coefficient, C_k, is the k^{th} coefficient of the inverse Fourier expansion,

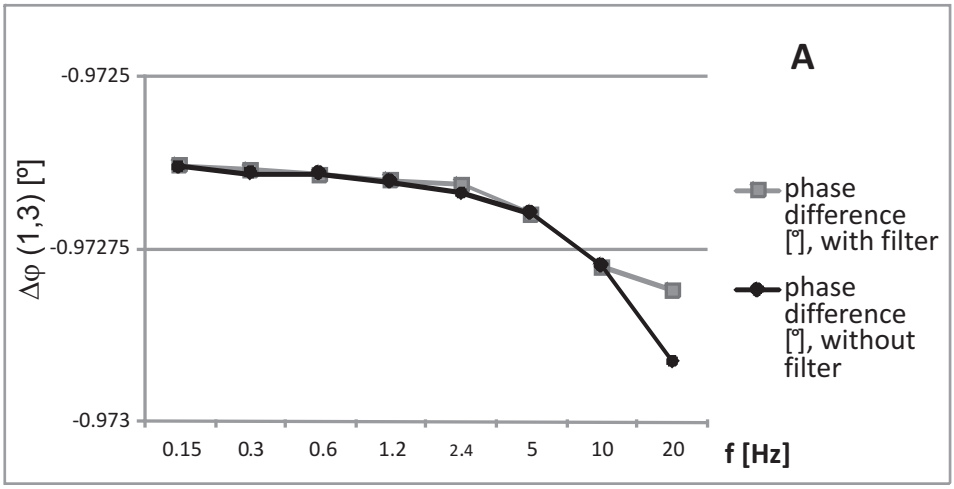

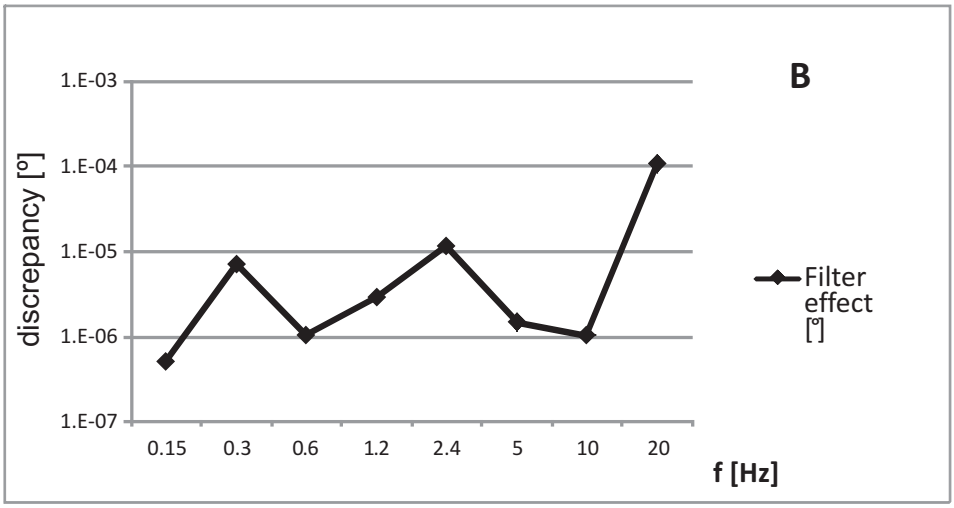

FIGURE 11 | **An illustration of industrial noise suppression. A) Phase difference, $\Delta\varphi_{1,3}$, for undistorted synthetic signal in two different cases: with linear filter applied and without linear filter applied. B) The discrepancy (arithmetical difference) between filtered and true response. We see that for frequencies below 10 Hz the discrepancy is smaller than 0.00002 ° which is negligibly small if compared to typical anomalous value of $\Delta\varphi_{1,3}$ (-0.5 ° - -5 °).**

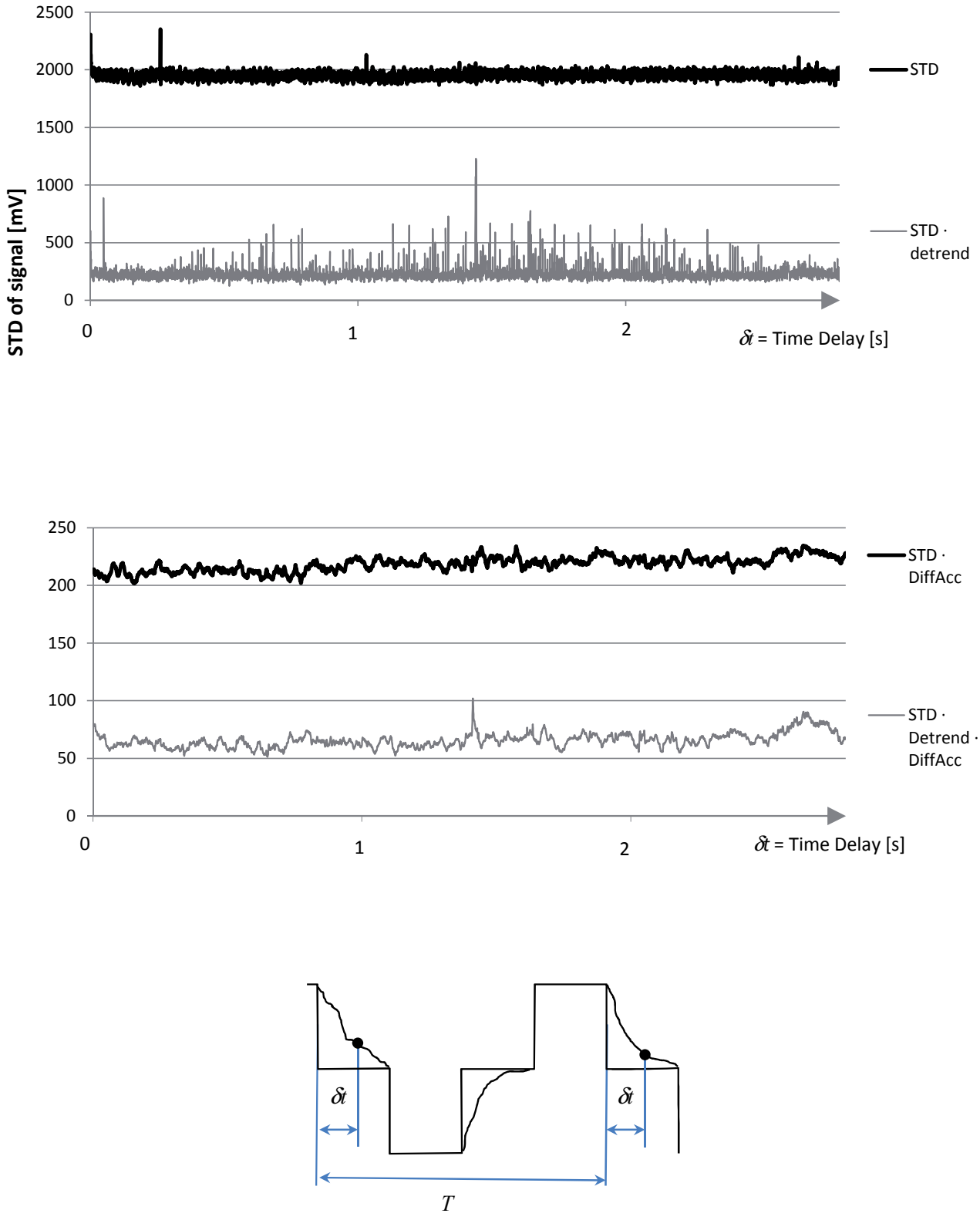

FIGURE 12 | **Detrend operation decreases the STD of the data 4-10 times. Shown at the upper panel are the STD of raw data (black) and the detrended data (grey) versus the time delay. The detrended data are about 10 times less than raw data. Shown at the lower panel are the STD of differentially accumulated data (black) and detrended and differentially accumulated data (grey) versus the time delay. The detrended data is about 4 times less than the original data. Shown at the right panel are the pulsed square-wave and the time delay, δt.**

$$M(t_n) = \sum_{k=1}^{N} C_k e^{-2\pi i n k/N} . \quad (25)$$

The coefficient is often called k^{th} harmonics. Since the carrier is an antiperiodic signal of known frequency, all we need are the odd harmonics, C_1, C_3, C_5, … Even harmonics and frequencies between harmonics represent noise for the CSEM case. One more consequence is that we can accumulate the response in the time domain before the use of the Fourier transform. This fact simplifies CSEM frequency analysis compared to the MT case. Operation (24) does not belong to the group of operations described above as it produces data of a different nature than the input data. However, we can perform some additional accumulation after Fourier transform, i.e., accumulation in the frequency domain.

Accumulation in frequency domain

As we obtained a series of estimates, F_1, F_2,…,F_r, of a frequency domain response function F (e.g., it can be any of the response functions (1)-(4)), we can perform an additional accumulation of the response. Arithmetic mean, $(F_1+F_2+\ldots+F_r)/r$, is the simplest accumulation type. In addition, Egbert and Booker (1986) showed that robust processing of electromagnetic data can substantially improve the processing over least squares methods. Apart from the arithmetic mean, we adopted three options of accumulation in the frequency domain:accumulation in the frequency domain:

1. median of values F_1, F_2,…,F_r;
2. trimmed mean of values F_1, F_2,…,F_r;
3. Hodges-Lehman estimate (Huber, 1981) of values F_1, F_2,…,F_r.

Although this operation requires performing longer measurements, it reduces the uncertainty of the estimated values.

Examples of processing

We use the field data acquired by Nord-West Limited for the rest of the analysis.

1) The IP survey was performed in Pechora province (Komi Republic, Russia) in 2006. These works resulted in the delineation of zones with anomalous IP values. Indicated anomalies in chargeability are twice as large as the background chargeability values (Fig. 13). Several productive oil wells (black circles in Fig. 13) have been drilled within the anomalies. An example of raw data and the result of processing are shown in Fig. 7 for the transmitter-receiver set-up shown in Fig. 10B. For this survey, the processing scheme was as follows: first, we removed the trend and industrial noise and then we performed robust differential accumulation, correction for the source signal amplitude drift and calculated the response functions. The upper panel of Fig. 8 shows typical voltage data of good quality from the survey area. The lower panel of the figure shows the result of processing applied to the same data. Fig. 7 shows raw data obtained at the 5-00-b observation site (lower panel) and log-log plots of time-domain IP responses processed from the data obtained at 6 observation sites located at the 5th profile of the survey area. IP responses of the same type were obtained at approximately 420 observation sites and became a basis for the IP chargeability map of the area shown in Fig. 13. It is seen in Fig. 7 that responses have been recovered remarkably well in as wide a range of values as possible (more than two orders of magnitude). We consider this a significant improvement since the raw data (see Fig. 3, 6, 7) were extremely noisy (noise/signal ratio was up to 1000).

2) Phase IP measurements were performed on the Kola Peninsula in 2004. The field set-up is shown in Fig. 10A. Half a dozen MARY-24 units (http://www.nw-geo.ru/index.php?a=1&b=2&c=2) were used as the receivers at two frequencies, 1.22 Hz and 0.3 Hz. A significant phase IP anomaly 20 m wide and 60 m long was revealed using phase difference $\Delta\varphi 1,3$ (see eq. (4)) that is shown in the lower panel of Fig. 9. Apparent resistivity and phase values show anomalous values at the same place (upper panel of Fig. 9). Large lateral gradients of phase and resistivity indicate that the top of the anomalous object is located very shallowly. A well bore was drilled later at the center of this anomaly and a 6 m deep massive ore deposit was found that consists mainly of titaniferous magnetite.

3) Joint IP and AMT (audiomagnetotelluric) field tests were conducted at Chernogorsk at the known deposit of sulphidized platinum-copper-nickel ore (Norilsk region, Russia) in 2005. Two RMCIP units collected IP data at lines MN = 100 m, and one line AB = 3 km was used as a source grounded wire. The field set-up is shown in Fig. 10A. The resulting map of apparent resistivity is shown in Fig. 14, upper panel; map of phase difference, $\Delta\varphi_{1,3}$, at 0.15 Hz is shown in Fig. 14, lower panel. Raw data obtained in this survey are presented in Fig. 4. The result of the field tests agreed with the geological data available in the region. More detailed geological and geophysical settings for the exploration can be found in Andreeva et al. (2006).

In case 1) we used a processing algorithm which can be expressed with the following formula

$$R(DNM) \circ g^a \circ g^c \circ g^a \circ g^i \circ g^d , \quad (26)$$

whereas in cases 2) and 3) we used a processing algorithm which can be expressed as

$$R(IP) \circ g^a \circ g^t \circ g^s \circ g^d , \quad (27)$$

provided that operations g^d, g^i, g^a, g^t, g^s, g^c, and $R(\cdot)$ are as follows: g^d stands for the detrend operation, g^i stands for the industrial noise suppression operation (whether 50 Hz or 60 Hz), g^a stands for the robust differential accumulation operation, g^t stands for the transient noise suppression operation, g^s stands for the induction spikes suppression operation and $R(\cdot)$ stands for the response function calculation module. Some ad hoc operations have also been elaborated and used, however they have not been documented here, e.g., correction, g^c, for the source amplitude drift (see Fig. 6, lower panel) due to frozen ground melting at the source electrode location.

SUMMARY

The focus of this work was elaboration of methods and software to process CSEM data. We analyzed the available field data and offered a classification of noises and distortions arising in practice. For each noise and distortion type, we offered an operation that should help overcome that particular noise or distortion. A summary of the noises/distortions is presented in Table 1.

We offer to build the processing algorithm as a composition of processing operations and a finalizing response function calculation module. Although several processing operations have been invented in this work, a focus was

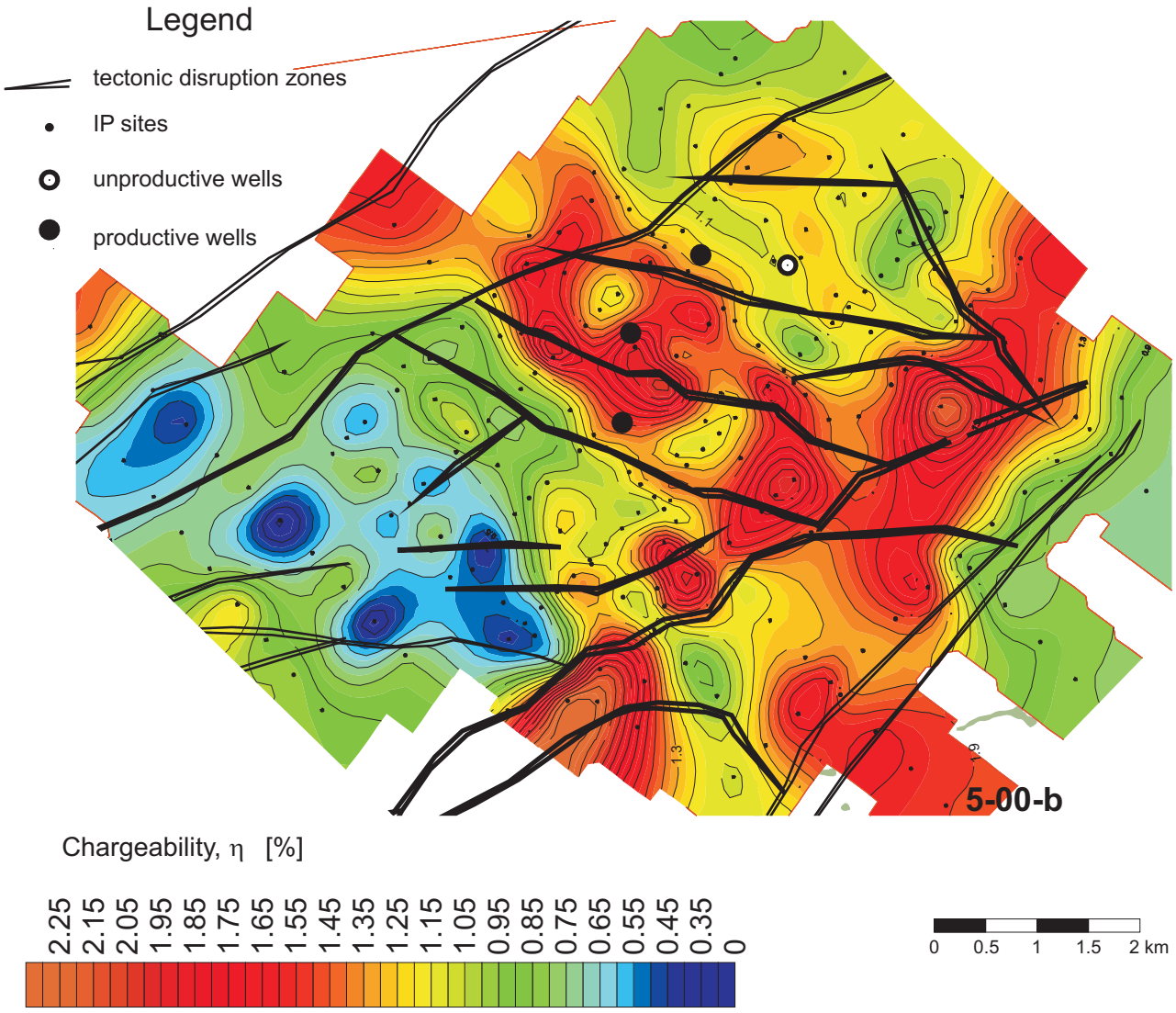

FIGURE 13 | **Chargeability map at Pechora province as if found from the measured voltage. Large chargeability values are shown in red and indicate an IP anomaly. Three well bores (black circles) drilled within the IP anomaly turned out to be productive as opposed to the fourth well bore (white circle) that was drilled beyond the anomaly.**

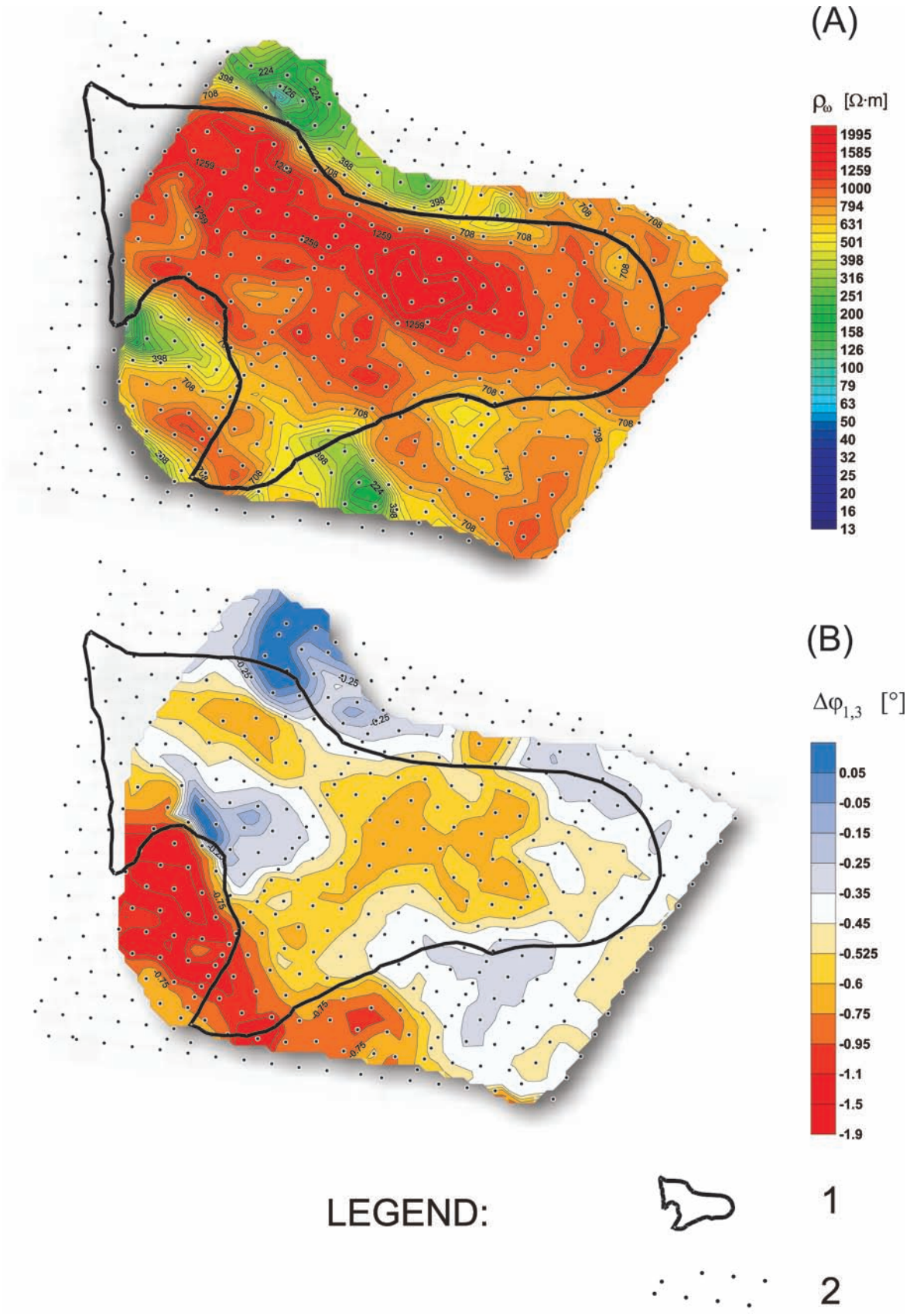

FIGURE 14 | **IP resistivity (A) and phase difference (B) maps obtained in Norilsk region during joint IP and AMT field tests. Key: 1. solid line delineates the location of Chernogorsk intrusion; 2. dots indicate IP observation sites.**

TABLE 1 | **Table relating the types of noise and distortions, opperations applied and data examples for each corresponding type.**

noise or distortion	respective operations	see raw survey data examples affected by this type of noise/distortion in:
trend	g^d, g^a	Fig. 3, 5-7
industrial noise	g^i, g^a	Fig. 2, 5
transient noise	g^t, g^a	Fig. 4b, c
induction spikes	g^s	Fig. 4a-c
source amplitude drift	g^c	Fig. 6, lower panel

made at free composition of the operations rather than the elaboration of new operations. We built a group of processing operations taking into account three requirements, processing operations must: 1) suppress noise and distortions arising in practice, 2) not distort true signal and 3) be freely composable with the other processing operations. Furthermore, we elaborated freely composable software modules which correspond to the basic processing operations belonging to the group. With the use of the software modules, we elaborated a number of software packages (Octopus Pro, DNM and others) and used them to process CSEM survey data. Our experience shows that even if an algorithm proved to be successful for one survey dataset, the algorithm can still be unsuccessful for another survey. If that is the case, an additional analysis of the data and processing operations adjustment can save the situation.

Another observation is that when we plot the first processing result at the survey map, the brightest anomalies mostly represent processing defects rather than the sought anomalies of resistivity, phase difference or other geophysical parameters. We recommend that the processing operator check the raw data at the location of the brightest anomalies for the noise level, presence of trends or industrial noise, and the source square-wave amplitude stability. If these unfavorable factors are present, we recommend modifying the parameters of the processing operations which constitute the processing algorithm. If this does not yield a result, we recommend composing another processing algorithm using our basic processing operations along with raw data analysis.

CONCLUSIONS

A suite of processing algorithms presented in this paper allows for recovering response functions of very good quality from extremely noisy data. The success of the processing is ensured by exploiting a special property of CSEM signal - its antiperiodicity. An important feature of the processing procedure is the possibility to easily merge one algorithm's operation with any other, which makes the suite adjustable to the type of data noise in a specific survey.

The algorithms were successfully applied to many survey datasets and show remarkable results in extracting the Earth's response from extremely noisy data.

The next challenging tasks are the design and employment of multichannel processing algorithms and advanced quality control algorithms.

ACKNOWLEDGMENTS

The authors are grateful to both referees (C. Manoj and X. Garcia) for their valuable suggestions and comments on the original manuscript. The authors would also like to thank Nord-West Limited for permission to publish the data and co-workers of the company for data collection and visualization of results as well as for numerous discussions. This work was supported in part by the Russian Foundation for Basic Research under grant Nº. 06-05-64329-a.

REFERENCES

Alekseev, D.A., Pankratov, O.V., Yakovlev, A.G., 2006. Joint electro-prospecting investigations at kimberlites in Western Yakutia using Phoenix equipment. Russia, Proceedings of 6th Phoenix Geophysics seminar at Alexandrovka, 11-15.

Andreeva, E.V., Bobachev, A.A., Varentsov, I.M., Vereschagina, M.P., Kulikov, V.A., Yakovlev, A.G., Yakovlev, D.V., 2006. Joint geophysical explorations for copper-nickel ore deposits of MMC Norilsk Nickel. Exploration and Protection of Mineral Resources (in Russian), 8, 71-79.

Chave, A.D., Constable, S.C., Edwards, R.N., 1991. Electrical exploration methods for the seafloor. The magnetometric resistivity method. In: Nabighian, M.N., (ed.). Electromagnetic methods in applied geophysics. Society of Exploration Geophysicists (SEG), Investigations in geophysics, 3, 931-966.

Davydycheva, S., Rykhlinski, N., Legeido, P., 2006. Electrical-prospecting method for hydrocarbon search using the induced-polarization effect. Geophysics, 71, G179-G189.

Edwards, R.N., Nabighian, M.N., 1991. The magnetometric resistivity method. In: Nabighian, M.N. (ed.). Electromagnetic methods in applied geophysics. Society of Exploration Geophysicists (SEG), Investigations in geophysics, 3, 47-104.

Egbert, G.D., Booker, J.R., 1986. Robust estimation of geomagnetic transfer functions. Geophysical Journal of the Royal Astronomical Society, 87, 173-194.

Huber, P., 1981. Robust Statistics. New York, Wiley, 320 pp.Ifeachor, E.C., Jervis, B.W., 2002. Digital Signal Processing - A Practical Approach. 2nd edition, New York, Prentice Hall, 933 pp.

Koefoed, O., 1979. Geosounding Principles, 1. Resistivity Sounding Measurements. Amsterdam, Elsevier Scientific Publishing Company, 276 pp.

Kulikov, A.V., Shemyakin, E.A., 1978. Electric survey using phase induced polarization method. Moscow, Nedra, 157 pp.

Kulikov, A.V., Zhilnikov, V.D., Sarbash, V.S., Shemyakin, E.A., Lemetz, V.I., Orlov, G.I., Goryunon, V.I., Deynehovskaya, N.A., 1975. Phase measurement for Induced Polarization method at alternate electric current. Alma-Ata, Kazakh subsidiary of VIRG (in Russian), 126 pp.

Nabighian, M.N., Macnae, J.C., 1991. Time domain electromagnetic prospecting methods. The magnetometric resistivity method. In: Nabighian, M.N. (ed.). Electromagnetic methods in applied geophysics. Society of Exploration Geophysicists (SEG), Investigations in geophysics, 3, 427-520.

Pushkarev, P.Y., Yakovlev, A.G., 2005. Induced polarization method. In: Khmelevskoy, V.K., Modin, I.N., Yakovlev, A.G. (eds.). Moscow, Electroprospecting (in Russian), 310 pp.

Sheriff, R., 2002. Encyclopedic Dictionary of Applied Geophysics. Society of Exploration Geophysicists, Geophysical Reference Series (4th edition), 429 pp.

Simpson, F., Bahr, K., 2005. Practical Magnetotellurics. Cambridge, Cambridge University Press, 270 pp.

Spies, B.R., Frischknecht, F.C., 1991. Electromagnitic sounding. In: Nabighian, M.N. (ed.). Electromagnetic methods in applied geophysics. Society of Exploration Geophysicists (SEG), Investigations in geophysics, 3, 285-425.

Strack, K.M., 1984. The deep transient electromagnetic sounding technique: first field test in Australia. Exploration Geophysics, 15, 251-259.

Strack, K.M., Hanstein, T.H., Eilenz, H.N., 1989. LOTEM data processing for areas with high cultural noise levels. Physics of the Earth and Planetary Interiors, 53, 261-269.

Velikhov, E.P (ed.), 1989. Geoelectric investigations in the Baltic shield with a powerful current source. Moscow, Nauka (in Russian), 272 pp.

Zhdanov, M.S., Keller, G., 1994. The Geoelectrical Methods in Geophysical Exploration: Elsevier, Amsterdam, 873 pp.

Zonge, K.L., Hughes, L.J., 1991. Controlled source audio-frequency magnetotellurics. The magnetometric resistivity method. In: Nabighian, M.N. (ed.). Electromagnetic methods in applied geophysics. Society of Exploration Geophysicists (SEG), Investigations in geophysics, 3, 713-809.

Manuscript received May 2007;
revision accepted November 2008;
published Online November 2009.